PNAS RESEARCH ARTICLE | CHEMISTRY

Phonon signatures for polaron formation in an anharmonic semiconductor

Feifan Wang[a,1], Weibin Chu[b,c,1], Lucas Huber[a], Teng Tu[d], Yanan Dai[a], Jue Wang[a], Hailin Peng[d], Jin Zhao[b,e,2], and X.-Y. Zhu[a,2]

Edited by Martin Zanni, University of Wisconsin-Madison, Madison, WI; received December 13, 2021; accepted May 20, 2022 by Editorial Board Member Shaul Mukamel

Mechanistic studies on lead halide perovskites (LHPs) in recent years have suggested charge carrier screening as partially responsible for long carrier diffusion lengths and lifetimes that are key to superior optoelectronic properties. These findings have led to the ferroelectric large polaron proposal, which attributes efficient charge carrier screening to the extended ordering of dipoles from symmetry-breaking unit cells that undergo local structural distortion and break inversion symmetry. It remains an open question whether this proposal applies in general to semiconductors with LHP-like anharmonic and dynamically disordered phonons. Here, we study electron-phonon coupling in Bi_2O_2Se, a semiconductor which bears resemblance to LHPs in ionic bonding, spin-orbit coupling, band transport with long carrier diffusion lengths and lifetimes, and phonon disorder as revealed by temperature-dependent Raman spectroscopy. Using coherent phonon spectroscopy, we show the strong coupling of an anharmonic phonon mode at 1.50 THz to photo-excited charge carriers, while the Raman excitation of this mode is symmetry-forbidden in the ground-state. Density functional theory calculations show that this mode, originating from the A_{1g} phonon of out-of-plane Bi/Se motion, gains oscillator strength from symmetry-lowering in polaron formation. Specifically, lattice distortion upon ultrafast charge localization results in extended ordering of symmetry-breaking unit cells and a planar polaron wavefunction, namely a two-dimensional polaron in a three-dimensional lattice. This study provides experimental and theoretical insights into charge interaction with anharmonic phonons in Bi_2O_2Se and suggests ferroelectric polaron formation may be a general principle for efficient charge carrier screening and for defect-tolerant semiconductors.

ferroelectric polarons | dynamic screening | bismuth oxyselenide | electron-phonon coupling | anharmonic phonons

Significance

Interaction of charge carriers with phonons is an intrinsic property of semiconductors and has been commonly treated as a perturbation in the harmonic approximation to the quasi-particle band picture. Recent discoveries in lead halide perovskites have challenged this traditional view, suggested efficient charge screening by dynamically disordered and anharmonic phonons, and cultivated the proposal of ferroelectric polaron formation as one of the keys to the success of these materials. The present study provides experimental and theoretical evidence for the ferroelectric polaron in Bi_2O_2Se and serves as a first step toward generalizing this principle for the discovery of defect-tolerant semiconductors in optoelectronics applications.

The development of semiconductor materials in optoelectronics has been guided by fundamental understanding of charge carrier and exciton dynamics. While the laborious approach of moving ever closer to perfection has served well the development of electronics and optoelectronics in use today, the rapid rise of solution-processed lead halide perovskites (LHPs) has challenged this norm (1–5). In contrast to crystalline perfection in Si or III-V semiconductors, LHPs feature extensive static and dynamic disorder, as expected from solution-processed materials with low free energies of formation. Studies in the last a few years have suggested the long carrier diffusion lengths and lifetimes in LHPs can be traced to their mixed covalent-ionic bonding characters that give rise to defect-tolerant bands structures (6–8) and highly polarizable lattices (1, 2, 3–5). The latter is most obviously reflected in the dielectric function, which features a large jump (~8× in $CH_3NH_3PbI_3$) as frequency decreases across the broad transverse optical (TO) phonon resonances at ~1 THz (9). The similarity of these dielectric functions to those of ferroelectric and paraelectric materials prompted Miyata and Zhu (9) to put forward the ferroelectric polaron proposal. In this model, electric field from a charge carrier induces local ordering of fluctuating dipoles from unit cells that undergo local structural distortion and break inversion symmetry, hereafter referred to simply as "symmetry-breaking." Alternatively, a free charge carrier may localize to transiently ordered domains of these symmetry-breaking unit cells. The result is the efficient screening of a charge carrier from scattering with other charge carriers and from charged defects, thus accounting for long carrier lifetimes and diffusion lengths. The dynamic localization of charge carriers in ferroelectric polaron formation in LHPs likely results in planar or "Belgian waffle"-shaped polaron wavefunctions (10), a hypothesis supported by ab initio molecular dynamics calculations (11). The key question we ask here is whether the ferroelectric polaron proposal is generally applicable to semiconductor materials other than LHPs, but featuring LHP-like phonon anharmonicity, dynamic disorder, and local symmetry breaking.

Author contributions: F.W., W.C., J.Z., and X.-Y.Z. designed research; F.W., W.C., L.H., T.T., Y.D., J.W., and J.Z. performed research; T.T. and H.P. contributed new reagents/analytic tools; F.W., W.C., L.H., Y.D., J.Z., and X.-Y.Z. analyzed data; F.W., W.C., Y.D., and X.-Y.Z. wrote the paper; and H.P. supervised the growth of sample crystal.

The authors declare no competing interest.

This article is a PNAS Direct Submission. M.Z. is a guest editor invited by the Editorial Board.

[1]F.W. and W.C. contributed equally to this work.

[2]To whom correspondence may be addressed. Email: zhaojin@ustc.edu.cn or xyzhu@columbia.edu.

This article contains supporting information online at http://www.pnas.org/lookup/suppl/doi:10.1073/pnas.2122436119/-/DCSupplemental.

Published July 21, 2022.

As the first step toward answering the above question, we investigate electron-phonon coupling in Bi_2O_2Se, a thermoelectric material (12) which has been recently recognized as a crystalline two-dimensional (2D) semiconductor (13) and successfully demonstrated in a broad range of electronic, optoelectronic, and thermoelectric devices with high efficiencies (14). Similar to LHPs, the Bi_2O_2Se crystal features mixed covalent and ionic bonding, with the latter between layers of $[Bi_2O_2]^{2+}$ and $[Se]^{2-}$ in each unit cell (Fig. 1*A*). The relatively large tetragonal unit cell in the I_4/mmm space group is centrosymmetric, but this symmetry is easily broken by strain, doping (15), or reduction in thickness of the flakes (16), leading to ferroelectricity. The susceptibility to symmetry-breaking is similar to the behavior of LHPs (10) and suggests the presence of multiple minima in corresponding phonon modes (17), giving rise to anharmonic and dynamically disordered phonons, as confirmed in temperature-dependent Raman spectra (see *Raman Spectroscopy Reveals Phonon Disorder*). The latter is responsible for the low thermoconductivity of Bi_2O_2Se (12, 14). The band structure of Bi_2O_2Se features an indirect bandgap of 0.8 eV ($X \rightarrow \Gamma$) and a direct gap of ~1.3 eV ($\Gamma \rightarrow \Gamma$) (13). Charge carrier transport in this material is band-like (13), and photophysical studies (18, 19) reveal sufficiently long carrier lifetimes and diffusion lengths responsible for efficient device performance (14). These properties bear resemblance to those in LHPs. Here, we probe polaron formation in Bi_2O_2Se by coherent phonon spectroscopy (CPS) with above gap optical excitation. In a CPS experiment, a short laser pulse excites coherent phonons either on the ground electronic state via an impulsive Raman mechanism (20) or on the excited electronic state via a displacive mechanism (21). The resulting coherent phonon is probed in the time domain from oscillations in reflectivity or absorbance of a probe laser pulse. This measurement is complemented by Raman spectroscopy showing the central peak behavior characteristic of phonon disorder. We carry out density functional theory (DFT) calculations in the presence of an extra electron, which is found to induce extended ordering of the symmetry-breaking unit cells in the anharmonic lattice.

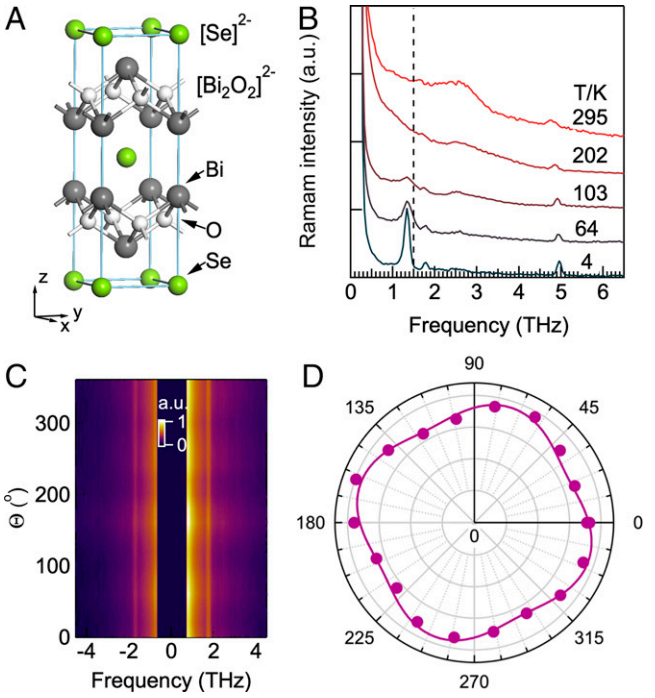

Fig. 1. Phonon disorder in Bi_2O_2Se revealed by Raman spectroscopy. (*A*) Structure of a Bi_2O_2Se unit cell. Gray, Bi; white, O; green, Se. (*B*) Raman spectra in the low frequency region at the indicated temperatures (4–295 K) obtained with cross polarizations (i.e., excitation and scattered light polarizations at $\alpha = 90°$). (*C*) Dependence of cross-polarized Raman spectra on the in-plane angle (θ) between excitation light and laboratory axis at a sample temperature of 104 K. (*D*) Polar plot of Raman intensity as a function of θ obtained from a vertical cut in (*C*) at 0.9 THz. The purple circles are data points and the line is fit to a sinusoidal function with a constant offset.

Raman Spectroscopy Reveals Phonon Disorder. Similar to LHPs (22), Bi_2O_2Se exhibits phonon liquid behavior (i.e., strong anharmonicity and dynamic disorder). This is shown by temperature-dependent Raman spectra in Fig. 1*B*. The spectrum at the lowest temperature (4 K) shows well-resolved phonon modes, including two at 1.35 and 1.77 THz in the low frequency range (see *SI Appendix*, Fig. S1 and Table S1 for detailed assignment). These low frequency phonon peaks broaden and/or diminish with increasing temperature and merge into a rising background toward zero frequency. The latter is the so-called central peak behavior (22) due to thermal fluctuations of the anharmonic and dynamically disordered lattice.

The disordered phonon environment is also reflected in the dependence of Raman intensity on the in-plane angle (θ) between excitation light and the crystalline axis. For harmonic modes at higher frequencies, such as the B_{1g} mode at 10.8 THz, the Raman peak intensity shows a $|1\text{-}\sin 4\theta|$ angular dependence (*SI Appendix*, Fig. S2), which reflects the fourfold crystalline symmetry. In contrast, the central peak shows a much weaker angular dependence (Fig. 1*C*), which can be described by a sum of 82% isotropic and 18% $|1\text{-}\sin 4\theta|$ components (Fig. 1*D* at 0.9 THz). The dominant isotropic component, irrespective of the underlying crystal symmetry, is consistent with phonon liquid behavior, as is observed for LHPs in the high temperature phases (22).

Coherent Phonon Excitation from Carrier Lattice Interaction. To investigate how charge carriers interact with such a phonon environment, we use coherent phonon spectroscopy, a technique particularly suited for the investigation of electron-phonon coupling and that has been successfully applied to LHPs (23–25). We use an above-gap laser pulse ($h\nu_1$, ~35 fs pulse width) to excite the Bi_2O_2Se single crystal normal to the exposed (001) surface and probe the transient reflectance change (ΔR) by $h\nu_2$ = 1.55 eV (~35 fs pulse width) at a small incident angle (~10°) from surface normal. Fig. 2*A* shows a representative transient reflectance trace at an excitation photon energy of $h\nu_1 = 2.26$ eV and a sample temperature of T = 90 K. On top of the ultrafast rise and nearly constant ΔR in this time window, there is clearly an oscillatory component. The former (incoherent background) results from the build-up and quasi-equilibration of excited carriers (*SI Appendix*, Note S1) and the latter is assigned to coherent phonons. After removing the incoherent background in a phenomenological model of a Gaussian convoluted with exponential decays (*SI Appendix*, Fig. S3), we carry out Fourier transform (FT) of the residue coherent signal and this gives the single-frequency mode centered at $\nu_{CP} = 1.50 \pm 0.05$ THz (Fig. 2*A*, *Inset*). A short-time window FT analysis (*SI Appendix*, Fig. S4) confirms that this coherent phonon frequency remains constant with time. The Fourier amplitude depends linearly on excitation laser pulse energy ≤ 0.5 mJ/cm^2, above which deviation from linearity is observed (Fig. 2*B*). Within experimental uncertainty, the coherent phonon frequency ν_{CP} shows little dependence on excitation pulse energy, sample temperature (90–216 K), or excitation photon energy ($h\nu_1 = 1.55$–2.43 eV), *SI Appendix*, Fig. S5.

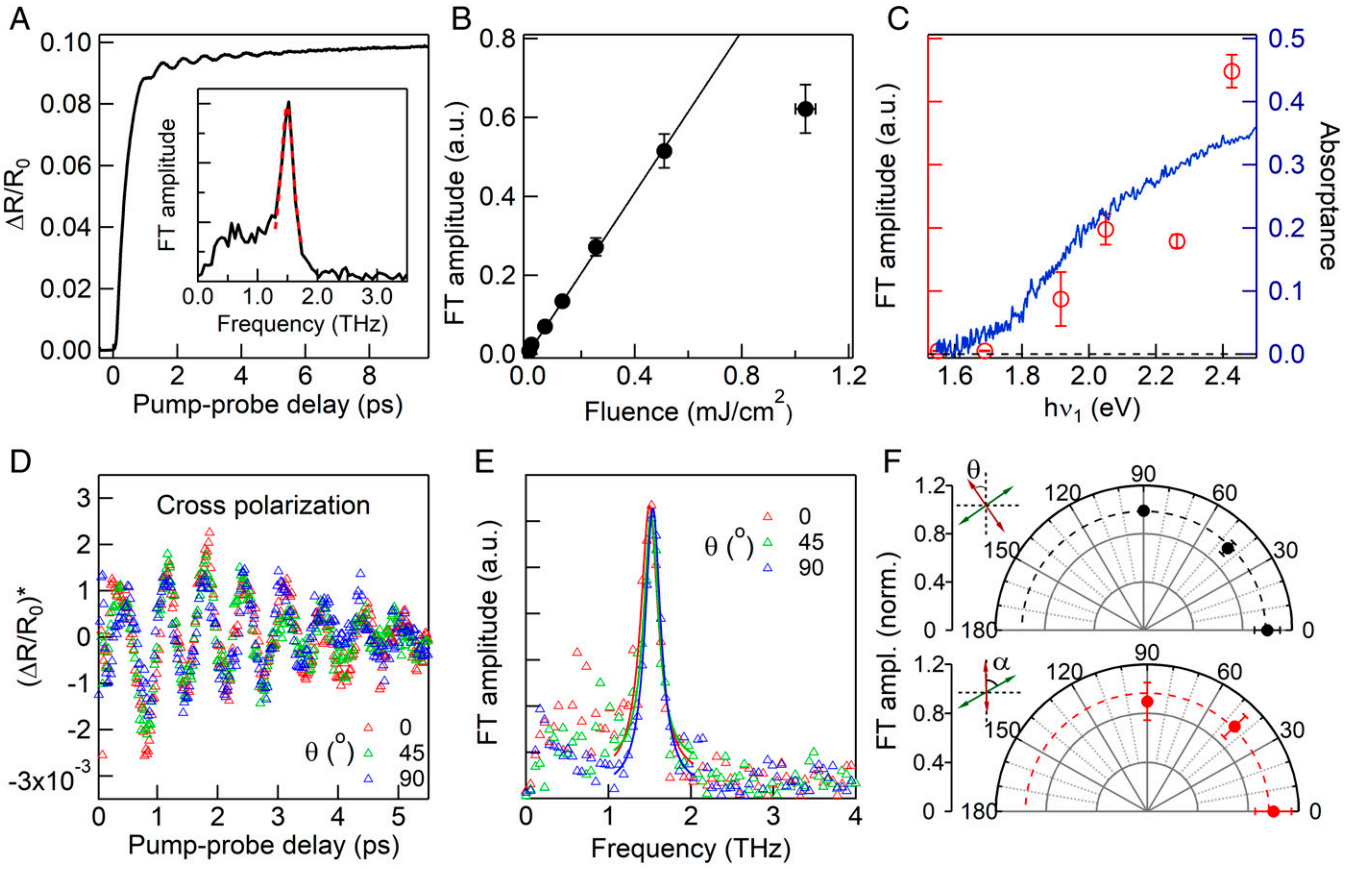

Fig. 2. Identification of the coupled phonon mode. (*A*) Transient reflectance ($\Delta R/R_0$) as a function of pump-probe delay. *Inset*: Fourier transform (black) of the oscillatory component and the red-dashed curve is a Gaussian fit, with gives a peak ν_{CP} = 1.50 ± 0.05 THz. (*B*) Fourier amplitude at ν_{CP} (black circles) as a function of pump laser pulse fluence. The line is linear fit to data points at fluences ≤0.5 mJ/cm^2. (*C*) Fourier amplitude at ν_{CP} (red circles, left axis) as a function of pump photon energy. Also shown is the absorption spectrum (blue, right axis) from a 7-nm thick Bi_2O_2Se flake. (*D*) Oscillatory parts of transient reflectance for cross-polarized (α = 90°) pump-probe at different angles (θ = 0°, 45°, 90°) between probe polarization and an in-plane crystalline axis. (*E*) Fourier transform of the transient reflectance traces in (*D*). (*F*) Polar plots of FT amplitude for θ = 0°, 45°, 90° at α = 90° (*Upper*) and for α = 0°, 45°, 90° at θ = 0°. In all panels except (*C*), the sample was pumped at $h\nu_1$ = 2.26 eV and probed at $h\nu_2$ = 1.55 eV. In (*C*), the pump photon energy was varied in the range of ν_1 = 1.55–2.43 eV. The sample temperature was 90 K.

The observed coherent phonon is likely associated with the electronically excited state in a displacive excitation mechanism, in which the potential minimum along a particular phonon coordinate is displaced in the excited state from that in the ground state (21). This displacement occurring on a short time scale due to photo carrier generation launches the coherent phonon, which in turn modulates the dielectric function and thus the reflectance seen here. Support for this assignment comes from the correlation between the excitation energy dependence in the amplitude of coherent phonon oscillation and the optical absorption spectrum (25) (Fig. 2*C*). The former was obtained from the Fourier amplitude at ν_{CP} under the condition of the same incident photon flux at different $h\nu_1$ above the bandgap. The latter was determined from a 7-nm thick Bi_2O_2Se crystal (see *SI Appendix*, Fig. S6 for details). The coherent phonon frequency of ν_{CP} = 1.50 ± 0.05 THz is absent in the ground state Raman spectrum (dashed line in Fig. 1*B*); as we discuss in the next two paragraphs, this mode is observed under the condition of normal light incidences and in the excited state due to symmetry breaking.

To understand the nature of the phonon mode observed in the CPS measurement, we carry out symmetry and polarization analysis. Since the coherent lattice vibration obeys the symmetry restriction of a Raman process (26, 27), the CP amplitude depends on the polarizations of the pump and probe electric fields following the Raman tensor associated with a particular mode. We first use a cross-polarization geometry (i.e., pump-probe polarization at α = 90°) and change the probe polarization angle with respect to an in-plane sample crystal axis, θ. Fig. 2*D* shows the oscillation parts of the transient reflectance profiles, with corresponding Fourier transforms in Fig. 2*E*, at θ = 0°, 45°, and 90°, respectively. Within experimental uncertainty, the transient reflectance profiles and the resulting coherent phonon spectra are independent of θ, as summarized in the polar plot for the Fourier amplitude (Fig. 2*F*, *Upper panel*). The same isotropic responses are also observed for a fixed θ, but varying pump-probe polarization angles α = 0°, 45°, and 90° (Fig. 2*F*, *Lower panel*, and *SI Appendix*, Fig. S7).

Considering the vertical incidence of the pump pulse to the sample (001) surface and the D_{4h} point group, the isotropic polarization dependences point to an out-of-plane vibrational mode, whose amplitude is invariant to the in-plane polarizations of the pump and probe light. DFT calculations indicate that, within this frequency range, there are no Raman active modes around 1.5 THz with out-of-plane motions allowed under the symmetry restriction (*I*4/*mmm*) and within the harmonic approximation on the ground electronic state (*SI Appendix*, Fig. S8). The lowest-energy Raman-active mode with out-of-plane motion is the A_{1g} breathing mode at 4.8 THz, which is confirmed in the Raman spectra in Fig. 1*B* (ν = 4.95–4.74 THz) but not observed in the coherent phonon spectra. The above analysis suggests that the observed coherent phonon at ν_{CP} = 1.50 ± 0.05 THz likely

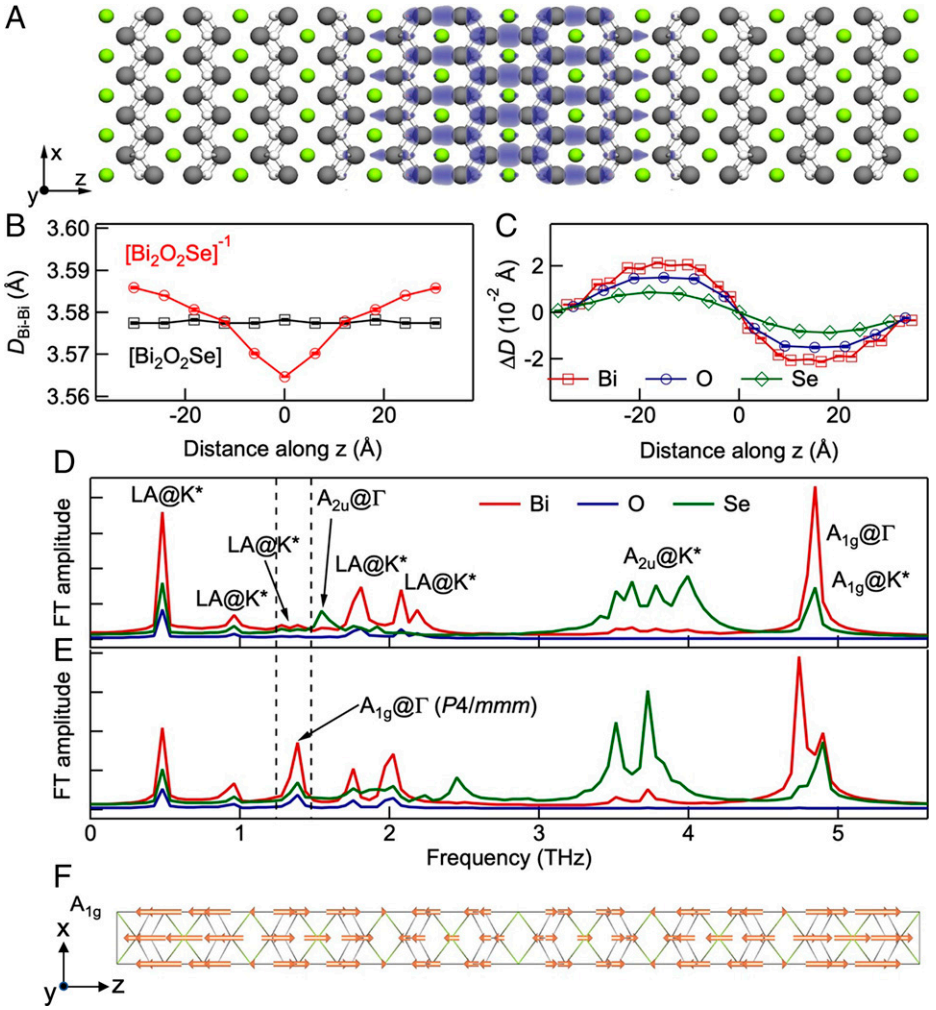

Fig. 3. Theoretical calculations of the electron polaron and phonon activities. (*A*) Distribution of the excess negative charge in a 4 × 4 × 6 simulation cell of $[Bi_2O_2Se]^{-1}$. Gray, Bi; white, O; green, Se. (*B*) The Bi-Bi distance between adjacent layers in the optimized geometries of ground state (black) and electron polaron (red). (*C*) The ionic displacements from the ground state in the electron polaron. The distance and displacement in (*B*) and (*C*) are average values from 16 unit-cells in the XY plane. Phonon spectra in AIMD for (*D*) neutral and (*E*) negatively charged Bi_2O_2Se at 50 K. The vibration spectra are calculated from the velocity autocorrelation function projected on the z-direction for each species. The corresponding phonon normal mode calculations are used to determine the peaks in (*D*) (*SI Appendix*, Note S3). As we used a large supercell in AIMD, the phonon from momentum space other than Γ are present in the simulated spectra, and these phonons are labeled with K*. The AIMD simulation for $Bi_2O_2Se^{-1}$ in (*E*) shows an A_{1g} mode at 1.4 THz introduced by the formation of the electron polaron. (*F*) The eigenvector of the signature A_{1g} mode. Se atoms on the even layers are stationary.

results from an out-of-plane vibrational mode which is nominally symmetry forbidden in the ground state under the vertical light incidence condition but becomes allowed in the presence of across gap carrier excitation. Note that the possibility of a surface phonon mode is ruled out by the correlation between coherent phonon amplitude and absorbance at different excitation photon energies ($h\nu_1 = 2.43 - 1.55$ eV) with different penetration depths ($2 - 60$ μm, *SI Appendix*, Fig. S6).

Theoretical Calculation of an Electron Polaron and Phonon Activities. To understand how photo carrier generation may result in a coherent phonon mode which is symmetry forbidden in the ground state, we implement DFT calculations in the presence of an excess charge. Hybrid functionals are employed to overcome well-known self-interaction error in DFT. Having benchmarked hybrid functionals (see *Methods* for details), we optimize the geometry of Bi_2O_2Se with an extra electron ($[Bi_2O_2Se]^{-1}$) using the PBE0 hybrid functional. To evaluate the finite-size effects, we use two different supercells (4 × 4 × 6 and 5 × 5 × 6, *SI Appendix*, Note S2). In either case, we find that the distribution of the excess negative charge changes from a delocalized character without lattice distortion to a localized distribution confined to a few layers (Fig. 3*A* and *SI Appendix*, Figs. S9 and S12). Structural analysis reveals that this localization originates from the σ bonding of Bi 6p orbitals, leading to a contraction of Bi-Bi distance between adjacent layers (Fig. 3*B* and *C*). Such lattice distortion accompanied by charge localization is consistent with the concept of self-trapping in polaron formation. The calculation yields polaron formation energies of 14.2 and 13.9 meV for the 4 × 4 × 6 and 5 × 5 × 6 simulation cells, respectively, while the corresponding electron quasi-particle energies are at 146 and 141 meV below the conduction band minimum (CBM), respectively. The large difference between the polaron formation energy and the electron quasi-particle energy indicates that most of the reduced electronic energy is compensated for by the increased lattice energy due to strain from symmetry breaking. The distribution of excess negative charge (Fig. 3*A* and *SI Appendix*, Fig. S12) reveals that this polaron is confined in the perpendicular direction but more delocalized in the 2D layer. The pseudo-2D character is confirmed from the examination of the spatial homogeneity of both lattice distortions and charge distribution in the in-plane periodic unit cells. In a

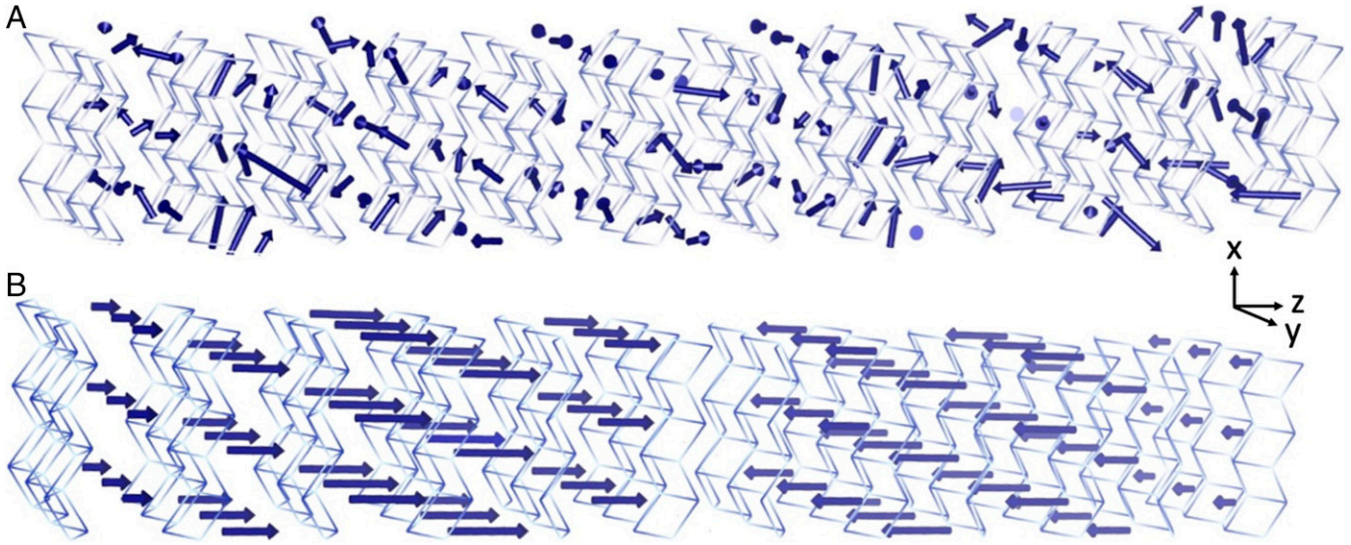

Fig. 4. Lattice fluctuations and possible local polar alignments. Schematic diagrams of the local dipoles calculated as the sum of the product between the displacements and formal charges of Bi/O/Se atoms in a unit cell. (*A*) Snapshot at a finite temperature simulated via MD and (*B*) for the optimized electron polaron from each ion in the unit cell with respect to the ground state optimized structure and q_i is the corresponding formal charge.

different context, similar 2D polarons have been proposed for electrons localized at the $SrTiO_3$ surface or $LaAlO_3/SrTiO_3$ interface (28–30). The 2D polaron configuration reduces the original *I*4/*mmm* symmetry and reorganizes the supercell (primarily composed of multiple *I*4/*mmm* cells) into a lower *P*4/*mmm* symmetry, while the lattice constants in the 2D layer remain unchanged with a = b = 3.90 Å. The symmetry-breaking of the 2D polaron explains the appearance of a Raman-active new phonon mode. We have also carried out DFT calculations of thin Bi_2O_2Se and $[Bi_2O_2Se]^{-1}$ structures with a minimum of four Bi layers in the horizontal direction and find that the anisotropic polaron still forms and retains its 2D shape (*SI Appendix*, Fig. S15).

To analyze the phonon activity associated with 2D polaron formation, we employ ab initio molecular dynamics (AIMD) simulation, which, unlike perturbation methods in the harmonic approximation, captures anharmonic effects based on ab initio potential energy surfaces. We determine the velocity autocorrelation functions projected in the z-direction from the AIMD simulations and carry out Fourier transform to obtain the phonon spectra. Fig. 3*D* and *E* present the calculated phonon spectra for neutral Bi_2O_2Se and the negatively charged $[Bi_2O_2Se]^{-1}$, respectively. The phonon peak around 1.4 THz arises distinctly in $[Bi_2O_2Se]^{-1}$, which is close to the experimentally observed coherent phonon frequency. To check the association between this phonon mode and polaron formation, we further calculate the normal modes and corresponding frequencies for both Bi_2O_2Se and $[Bi_2O_2Se]^{-1}$ with optimized geometries (*SI Appendix*, Notes S3 and S4). We find a new mode at 1.50 THz, which is absent in Bi_2O_2Se but appears in $[Bi_2O_2Se]^{-1}$ due to symmetry lowering upon electron polaron formation. The polarization vector of this new mode in $[Bi_2O_2Se]^{-1}$ (Fig. 3*F*) is consistent with A_{1g} symmetry. The frequency of this A_{1g} mode from normal mode analysis is in excellent agreement with the experimentally observed coherent phonon frequency and is close to that from AIMD simulation. Upon the injection of an electron, the energetically favorable state of the system is associated with the 2D-shaped polaron. The accompanying lattice distortion reduces the space group symmetry and increases the size of the unit cell. This allows the expression of a symmetry-breaking A_{1g} mode that is forbidden in the high-symmetry ground state. Therefore, the observation of the unprecedented A_{1g} mode in both experiments and simulations may represent signatures for polaron formation in Bi_2O_2Se.

Further insight into the electron polaron can be obtained from calculation of local dipoles in the AIMD simulation at finite temperatures. Fig. 4*A* shows a snapshot from the ground-state MD simulation showing the random orientations and fluctuations of local dipoles at every instant. The energy barrier between the local distorted and undistorted structures is estimated ~4.3 meV, which is less than k_BT at 50 K (k_B is the Boltzmann constant), leading to a fluctuating landscape of local dipoles in the Bi_2O_2Se lattice. When an electron is added to the system (Fig. 4*B*), the optimized structure shows that the local dipoles align along the *z* axis over a few nanometers and are extended over multiple unit cells in the x-y plane, forming a 2D electron polaron. It is this local dipolar ordering (i.e., ferroelectric polaron formation), which provides efficient Coulomb screening in the 2D plane of the charge carrier in Bi_2O_2Se.

In the present study, the excitation photon energy is ~1 eV above the direct gap of 1.3 eV and the initial excitation creates electrons/holes with excess energy that cool-down with intra- and interband relaxation via the emission of optical phonons. Using time-resolved two photon photoemission spectroscopy (*SI Appendix*, Fig. S11), we have directly determined the hot electron cooling dynamics in the conduction band in the Γ valley of Bi_2O_2Se. The hot electron cooling time constants are determined to be 0.5 ps and 0.4 ps, with initial energy relaxation rates of 0.32 eV/ps and 0.57 eV/ps, at T = 294 K and 112 K, respectively. These hot electron cooling rates are similar to those observed in a layered polar semiconductor In_2Se_3 featuring efficient polaron screening (31) and slightly slower than those in conventional polar crystalline semiconductor, such as GaAs (32). Note that the proposed ferroelectric polaron formation occurs for both hot and band-edge carriers (4, 33) that are not distinguished in the coherent phonon measurements presented above. The polaron formation time is not resolved here but must be of the order of ~100 fs to exert a sufficiently short disturbance and launch the coherent phonons.

Local symmetry breaking and anisotropic polaron formation observed here for Bi_2O_2Se and proposed earlier for LHPs (9, 10) may not be unique. For example, $SrTiO_3$ is characterized by the quantum paraelectric ground state, where dipole fluctuation

prevents long-range ordering even to 0 K (34). This phenomenon results from quantum tunneling through a low energy barrier between the symmetric/nonpolar and symmetry-breaking/polar structures. The fluctuating dipoles may be transiently ordered into the ferroelectric phase by strong electric field of a THz pulse (35) or strain from an optical pulse (36). Alternatively, electric field from a charge carrier can readily induce lattice polarization, forming the so-called "superparaelectric large polarons" (37). The coupling of an electron to anharmonic phonon modes and interaction with polar nanodomains (37–39) has long been considered as important to charge transport. Thus, the ferroelectric polaron (9, 10) is likely of general significance to charge carrier screening in a broad class of crystalline solids characterized by anharmonic, symmetry-breaking, and dynamically disordered phonons, leading to improved optoelectronic properties.

Methods

Details are available in *SI Appendix*. The Bi_2O_2Se single crystals are synthesized by a modified Bridgman method. Coherent phonon spectroscopy measurements are carried out with balanced detection, tunable femtosecond laser pump, and single-color femtosecond laser probe. The Raman scattering measurements are carried out on a home-built microscope with 1,064 nm CW laser excitation. The DFT calculation of polarons includes self-interaction error correction. The nonequilibrium dynamics of coupled electrons and nuclei are simulated by Ab initio Molecular Dynamics.

Data Availability. All study data are included in the article and/or *SI Appendix*.

ACKNOWLEDGMENTS. X.Z. acknowledges support for the Raman spectroscopy and coherent phonon spectroscopy from the Vannevar Bush Faculty Fellowship through Office of Naval Research (N00014-18-1-2080). The time-resolved two-photon photoemission experiments were supported by the Materials Science and Engineering Research Center (MRSEC) through the National Science Foundation (DMR-2011738).

Author affiliations: [a]Department of Chemistry, Columbia University, New York, NY 10027; [b]ICQD/Hefei National Laboratory for Physical Sciences at Microscale, CAS Key Laboratory of Strongly-Coupled Quantum Matter Physics, Department of Physics, University of Science and Technology of China, Hefei, 230026, China; [c]Department of Chemistry, University of Southern California, Los Angeles, CA 90089; [d]Center for Nanochemistry, Beijing Science and Engineering Center for Nanocarbons, Beijing National Laboratory for Molecular Sciences, College of Chemistry and Molecular Engineering, Peking University, Beijing 100871, China; and [e]Synergetic Innovation Center of Quantum Information & Quantum Physics, University of Science and Technology of China, Hefei, 230026, China

1. Y. Guo *et al.*, Dynamic emission Stokes shift and liquid-like dielectric solvation of band edge carriers in lead-halide perovskites. *Nat. Commun.* **10**, 1175 (2019).
2. C. Katan, A. D. Mohite, J. Even, Entropy in halide perovskites. *Nat. Mater.* **17**, 377–379 (2018).
3. L. M. Herz, How lattice dynamics moderate the electronic properties of metal-halide perovskites. *J. Phys. Chem. Lett.* **9**, 6853–6863 (2018).
4. H. Zhu *et al.*, Screening in crystalline liquids protects energetic carriers in hybrid perovskites. *Science* **353**, 1409–1413 (2016).
5. I. Anusca *et al.*, Dielectric response: Answer to many questions in the methylammonium lead halide solar cell absorbers. *Adv. Energy Mater.* **7**, 1700600 (2017).
6. W.-J. Yin, T. Shi, Y. Yan, Unusual defect physics in $CH_3NH_3PbI_3$ perovskite solar cell absorber. *Appl. Phys. Lett.* **104**, 063903 (2014).
7. D. Meggiolaro *et al.*, Iodine chemistry determines the defect tolerance of lead-halide perovskites. *Energy Environ. Sci.* **11**, 702–713 (2018).
8. X. Zhang, M. E. Turiansky, C. G. Van de Walle, Correctly assessing defect tolerance in halide perovskites. *J. Phys. Chem. C* **124**, 6022–6027 (2020).
9. K. Miyata, X.-Y. Zhu, Ferroelectric large polarons. *Nat. Mater.* **17**, 379–381 (2018).
10. F. Wang *et al.*, Solvated electrons in solids-ferroelectric large polarons in lead halide perovskites. *J. Am. Chem. Soc.* **143**, 5–16 (2021).
11. F. Ambrosio, J. Wiktor, F. De Angelis, A. Pasquarello, Origin of low electron–hole recombination rate in metal halide perovskites. *Energy Environ. Sci.* **11**, 101–105 (2018).
12. P. Ruleova *et al.*, Thermoelectric properties of Bi_2O_2Se. *Mater. Chem. Phys.* **119**, 299–302 (2010).
13. J. Wu *et al.*, High electron mobility and quantum oscillations in non-encapsulated ultrathin semiconducting Bi_2O_2Se. *Nat. Nanotechnol.* **12**, 530–534 (2017).
14. T. Li, H. Peng, 2D Bi_2O_2Se: An emerging material platform for the next-generation electronic industry. *Acc. Mater. Res.* **2**, 842–853 (2021).
15. M. Wu, X. C. Zeng, Bismuth oxychalcogenides: A new class of ferroelectric/ferroelastic materials with ultra high mobility. *Nano Lett.* **17**, 6309–6314 (2017).
16. T. Ghosh *et al.*, Ultrathin free-standing nanosheets of Bi_2O_2Se: Room temperature ferroelectricity in self-assembled charged layered heterostructure. *Nano Lett.* **19**, 5703–5709 (2019).
17. A. Marronnier *et al.*, Structural instabilities related to highly anharmonic phonons in halide perovskites. *J. Phys. Chem. Lett.* **8**, 2659–2665 (2017).
18. C. Zhu *et al.*, Observation of bimolecular recombination in high mobility semiconductor Bi_2O_2Se using ultrafast spectroscopy. *Appl. Phys. Lett.* **113**, 61104 (2018).
19. S. Liu *et al.*, Optical properties and photocarrier dynamics of Bi_2O_2Se monolayer and nanoplates. *Adv. Opt. Mater.* **8**, 1901567 (2020).
20. T. K. Cheng *et al.*, Impulsive excitation of coherent phonons observed in reflection in bismuth and antimony. *Appl. Phys. Lett.* **57**, 1004–1006 (1990).
21. H. J. Zeiger *et al.*, Theory for displacive excitation of coherent phonons. *Phys. Rev. B Condens. Matter* **45**, 768–778 (1992).
22. O. Yaffe *et al.*, Local polar fluctuations in lead halide perovskite crystals. *Phys. Rev. Lett.* **118**, 136001 (2017).
23. D. M. Monahan *et al.*, Room-temperature coherent optical phonon in 2D electronic spectra of $CH_3NH_3PbI_3$ perovskite as a possible cooling bottleneck. *J. Phys. Chem. Lett.* **8**, 3211–3215 (2017).
24. G. Batignani *et al.*, Probing femtosecond lattice displacement upon photo-carrier generation in lead halide perovskite. *Nat. Commun.* **9**, 1971 (2018).
25. F. Thouin *et al.*, Phonon coherences reveal the polaronic character of excitons in two-dimensional lead halide perovskites. *Nat. Mater.* **18**, 349–356 (2019).
26. T. E. Stevens, J. Kuhl, R. Merlin, Coherent phonon generation and the two stimulated Raman tensors. *Phys. Rev. B Condens. Matter Mater. Phys.* **65**, 144304 (2002).
27. G. A. Garrett, T. F. Albrecht, J. F. Whitaker, R. Merlin, Coherent THz phonons driven by light pulses and the Sb problem: What is the mechanism? *Phys. Rev. Lett.* **77**, 3661–3664 (1996).
28. C. Chen, J. Avila, E. Frantzeskakis, A. Levy, M. C. Asensio, Observation of a two-dimensional liquid of Fröhlich polarons at the bare SrTiO3 surface. *Nat. Commun.* **6**, 8585 (2015).
29. C. Cancellieri *et al.*, Polaronic metal state at the $LaAlO_3/SrTiO_3$ interface. *Nat. Commun.* **7**, 10386 (2016).
30. Z. Wang *et al.*, Tailoring the nature and strength of electron-phonon interactions in the $SrTiO_3$(001) 2D electron liquid. *Nat. Mater.* **15**, 835–839 (2016).
31. Y. Dai, M. E. Ziffer, X.-Y. Zhu, Screening of hot electrons in the ferroelectric semiconductor In_2Se_3. *Phys. Rev. B* **102**, 195201 (2020).
32. J. Sjakste *et al.*, Energy relaxation mechanism of hot-electron ensembles in GaAs: Theoretical and experimental study of its temperature dependence. *Phys. Rev. B* **97**, 064302 (2018).
33. P. P. Joshi, S. F. Maehrlein, X. Zhu, Dynamic screening and slow cooling of hot carriers in lead halide perovskites. *Adv. Mater.* **31**, e1803054 (2019).
34. K. A. Müller, H. Burkard, SrTiO3: An intrinsic quantum paraelectric below 4 K. *Phys. Rev. B* **19**, 3593–3602 (1979).
35. X. Li *et al.*, Terahertz field-induced ferroelectricity in quantum paraelectric $SrTiO_3$. *Science* **364**, 1079–1082 (2019).
36. T. F. Nova, A. S. Disa, M. Fechner, A. Cavalleri, Metastable ferroelectricity in optically strained $SrTiO_3$. *Science* **364**, 1075–1079 (2019).
37. K. Nasu, Photogeneration of superparaelectric large polarons in dielectrics with soft anharmonic T1u phonons. *Phys. Rev. B Condens. Matter Mater. Phys.* **67**, 1–8 (2003).
38. S. H. Wemple, M. DiDomenico Jr., A. Jayaraman, Electron scattering in perovskite-oxide ferroelectric semiconductors. *Phys. Rev.* **180**, 547 (1969).
39. J. D. Zook, T. N. Casselman, Electro-optic effects in paraelectric perovskites. *Phys. Rev. Lett.* **17**, 960 (1966).